ENGINEERING

Nanoscale 3D printing of glass photonic crystals with near-unity reflectance in the visible spectrum

Wang Zhang[1,2]†, Hongtao Wang[1]†, Hao Wang[3,4], Son Tung Ha[5], Lei Chen[1,6], Xue Liang Li[1], Cheng-Feng Pan[1,7], Bochang Wu[1,7], Md. Abdur Rahman[1], Yujie Ke[8], Qifeng Ruan[9], Xiaolong Yang[10], Thomas Christensen[11]*, Joel K. W. Yang[1,2,12]*

Glass is widely used as an optical material due to its high transparency, thermal stability, and mechanical properties. The ability to fabricate and sculpt glass at the nanoscale would naturally expand its application domain in nanophotonics. Here, we report an approach to print glass in three dimensions with nanoscale resolutions. We developed Glass-Nano, an organic-inorganic hybrid resin containing silicon elements. Using this high-resolution resin, three-dimensional (3D) photonic crystals (PhCs) were printed with two-photon lithography. After printing, the structures were heated to high temperatures in air to remove organic components and convert the remaining material into silica glass. 3D glass PhCs with periodicities as small as 260 nanometers were obtained after sintering at 650°C. The 3D glass PhCs exhibit ~100% reflectance in the visible range, surpassing the typical reflectances observed from similar structures in low–refractive index materials. The quality of PhCs achieved is observed in both electron microscopy and the excellent agreement with band structure calculations of idealized structures.

INTRODUCTION

As a structural material, glass stands out for its high transparency, mechanical strength, and thermal and chemical stability. High-resolution, three-dimensional (3D) printing of glass can extend the use of glass to an even broader range of applications beyond its current, already very broad, domain. At the macroscale, 3D glass structures can be printed via lithography using hybrid resins composed of silica nanoparticles and photo-curable monomers, followed by debinding at high temperatures to remove the organic components (*1*, *2*). At the microscale, two-photon polymerization lithography (TPL) was introduced for printing with these hybrid resins. Different micrometer-scale glass structures such as optical resonators (*3*) and microlenses (*4*) have been fabricated using this strategy. More recently, covalently bonded silicon has been introduced to print glass with submicrometer features (*5*–*9*), lowering the debinding temperature from ~1300°C to below 1000°C. Despite these achievements, fabricating glass structures with a submicrometer pitch (period) in all three dimensions remains a challenge.

A central motivation for pursuing submicrometer pitch in 3D glass structures is to explore applications in nanophotonics, especially within the visible spectrum. Photonic crystals (PhCs) exemplify these opportunities well, requiring periodicities at a fraction of the target wavelength. Traditionally, PhCs have been fabricated by stimulated emission depletion (STED) lithography (*10*–*12*) or self-assembly (*13*, *14*). However, these methods suffer from fabrication errors, such as nonuniformity, and limitations in PhC designs inherent to self-assembly approaches. As a result, the optical performance of previously realized visible-spectrum PhCs has usually been limited, with a relatively low reflectance (*10*, *15*–*18*). On the other hand, heat-induced shrinking-based TPL (*19*, *20*) is a promising approach to printing high-quality 3D structures with resolution below the diffraction limit (*10*, *21*). Our recent work (*22*) on the heat shrinkage of the Ti-Nano resin achieved a ~180-nm pitch in 3D high–refractive index (RI) titania structures, featuring a full photonic bandgap in the visible spectrum. However, the optical properties of nanoscale 3D low-RI structures in the visible range have not been fully studied due to the lack of fabrication methods. These low-RI materials have several advantages over high-RI materials such as an easy fabrication process from standard lithography of polymers (*23*–*25*), compatibility with other devices like optical fibers (*26*), and diverse applications, such as stretchable sensors (*27*, *28*) and electronics (*29*–*31*) that are based on low-RI materials. Enhancing the optical performance of low-RI PhCs can benefit various devices, including improving signal strength in flexible optical sensors (*32*) and enabling better light confinement in optical waveguides (*33*).

In this work, we introduce a high-resolution resin, Glass-Nano, that enables TPL printing of low-RI 3D glass PhCs. After printing, we heat the structures at high temperatures to remove the organic components and further convert the material into silica glass. Structures with periodicities as small as 260 nm are achieved. We characterize the optical properties of these low-RI PhCs through reflectance measurements. Notably, we observe nearly 100% reflectance within a substantial range of incidence angles. Angle-resolved measurements and band structure analysis are used to explain the observation of high reflectance in these low-RI 3D PhCs. Crucially, we

[1]Engineering Product Development, Singapore University of Technology and Design, Singapore 487372, Singapore. [2]Singapore-HUJ Alliance for Research and Enterprise (SHARE), The Smart Grippers for Soft Robotics (SGSR) Programme, Campus for Research Excellence and Technological Enterprise (CREATE), Singapore 138602, Singapore. [3]School of Instrumentation and Optoelectronic Engineering, Beihang University, Beijing 100191 China. [4]Hangzhou International Innovation Institute, Beihang University, Hangzhou 311115, China. [5]Institute of Materials Research and Engineering (IMRE), Agency for Science, Technology and Research (A*STAR), 2 Fusionopolis Way, Innovis #08-03, Singapore 138634, Singapore. [6]College of Mechanical and Vehicle Engineering, Hunan University, Changsha 410082, China. [7]Department of Electrical and Computer Engineering, National University of Singapore (NUS), 4 Engineering Drive 3, Singapore 117576, Singapore. [8]School of Interdisciplinary Studies, Lingnan University, Tuen Mun, Hong Kong SAR, China. [9]Ministry of Industry and Information Technology Key Lab of Micro-Nano Optoelectronic Information System, Harbin Institute of Technology (Shenzhen), Shenzhen 518055, China. [10]College of Mechanical and Electrical Engineering, Nanjing University of Aeronautics and Astronautics, Nanjing 210016, China. [11]Department of Electrical and Photonics Engineering, Technical University of Denmark, Kongens Lyngby 2800, Denmark. [12]POLIMA—Center for Polariton-driven Light–Matter Interactions, University of Southern Denmark, Campusvej 55, DK-5230 Odense M, Denmark.
*Corresponding author. Email: thomas@dtu.dk (T.C.); joel_yang@sutd.edu.sg (J.K.W.Y.)
†These authors contributed equally to this work.

obtained excellent agreement between measured reflectances and band structure calculations of idealized structures, down to matching the spectral ripples on the long wavelength side of the bandgap.

RESULTS

The main composition of the Glass-Nano resin is presented in Fig. 1A (Materials and Methods). The resin contains an acryloxy-propyl polyoctahedral silsesquioxanes (POSS) cage mixture (MA0736) (*7*) as the silicon precursor. The multibranched acrylate groups in MA0736 can be directly polymerized, dispersing the silicon elements throughout the polymer structure upon curing. Bisphenol A ethoxylate diacrylate (BPADA) was added as a cross-linker to increase the RI (*22*, *34*) of the resin. Pentaerythritol triacrylate (PETA) (*20*) was adopted as another cross-linker to facilitate the polymerization and enhance the mechanical properties of the printed structures. Toluene was added as a solvent to dissolve the high-efficiency TPL initiator 7-diethylamino-3-thenoylcoumarin (DETC) (*35*). See the Supplementary Materials for a more detailed discussion of the general design strategy for the Glass-Nano resin.

TPL (*24*, *25*, *36*–*38*) with the Photonic Professional GT2 from Nanoscribe GmbH was used to pattern the resin into polymer-silicon hybrid 3D PhCs (Fig. 1B and Materials and Methods). The RI of the resin was intentionally tuned to ~1.52 (Supplementary Materials) for index matching with the microscope objective at the excitation wavelength of 780 nm, leading to an optimized print resolution of TPL (*34*). After printing and sintering in air, the polymer inside the PhC is removed, and the print transforms into a silica glass PhC as the silicon element inside the printed structures oxidizes at high temperatures. Using the customized Glass-Nano resin for printing (Materials and Methods), a typical as-printed PhC features a pitch of ~1.7 μm (Fig. 1C). After sintering at 650°C, the pitch shrinks to ~350 nm (Fig. 1D), resulting in a ~4.9-fold reduction per linear dimension and ~118-fold shrinkage in volume. See fig. S2 for a comparison of the scales before and after sintering using consistent magnification. By tuning the pitch of the as-printed PhCs, different 3D structural colors (*19*, *39*–*41*) can be obtained (Fig. 1E) after sintering. Notably, the normal-incidence reflectance spectra of these structures exhibit peaks that approach ~100% in the visible range, depending on pitch (Fig. 1F).

Thermogravimetric analysis (TGA) of a bulk sample cured under ultraviolet light was conducted to determine the decomposition temperature of the organic components in the as-printed structures. Derivative weight loss peaks at 422° and 527°C indicate the two primary decomposition temperatures of the polymer in air (Fig. 2A). Above 625°C, no further mass reduction was observed, indicating the complete removal of the organic components. No further shrinkage was observed above 650°C until 900°C (fig. S3). Hence, we used a temperature of 650°C to remove the organic composition in all further results presented here. Note that the structure may undergo further shrinkage due to densification, crystallization, or melting at higher temperatures (*22*). The chemical decomposition of the material in air at various temperatures can be analyzed using mass spectrometry (*7*). X-ray photoelectron spectroscopy (XPS) and Fourier transform infrared (FTIR) spectroscopy confirm the high purity of the sintered materials compared to the standard glass

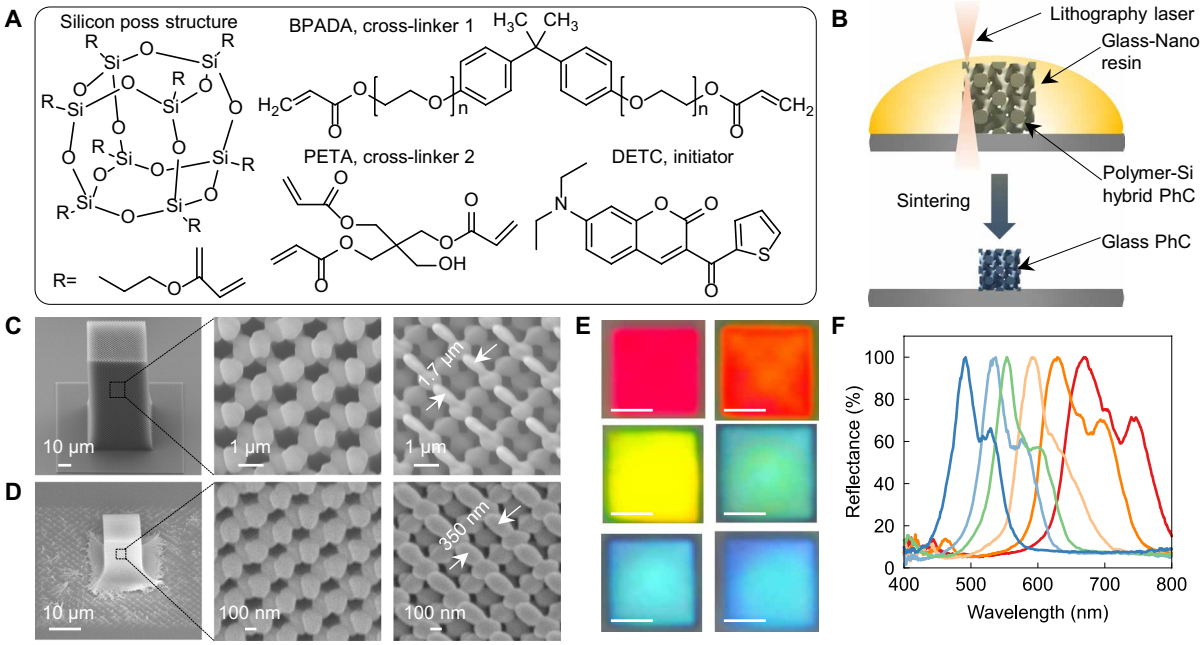

Fig. 1. Resin formulation, fabrication, and optical measurements. (**A**) Main chemical composition of the Glass-Nano resin. Toluene was added to the resin to dissolve the initiator (methods). (**B**) Schematic of the printing and sintering process. TPL was used to polymerize the resin to 3D microstructure. After printing, the structure was heated in air to remove the organic composition, and oxygen reacts with silicon within the structure to form silica. (**C** and **D**) Tilt view (left), high-magnification tilt view (middle), and top view (right) scanning electron microscope (SEM) images of the as-printed (C) and sintered (D) diamond PhCs. The PhC in (C) has 20 units in the lateral direction and 40 units in the vertical direction. (**E**) Optical micrographs of the sintered diamond PhCs with different pitches. Scale bars in (E), 5 μm. (**F**) Measured absolute reflectance spectra of the corresponding PhCs in (E) using a 10× objective lens with a numerical aperture (NA) of 0.3. The reflectance of spectra was normalized to a silver mirror reference.

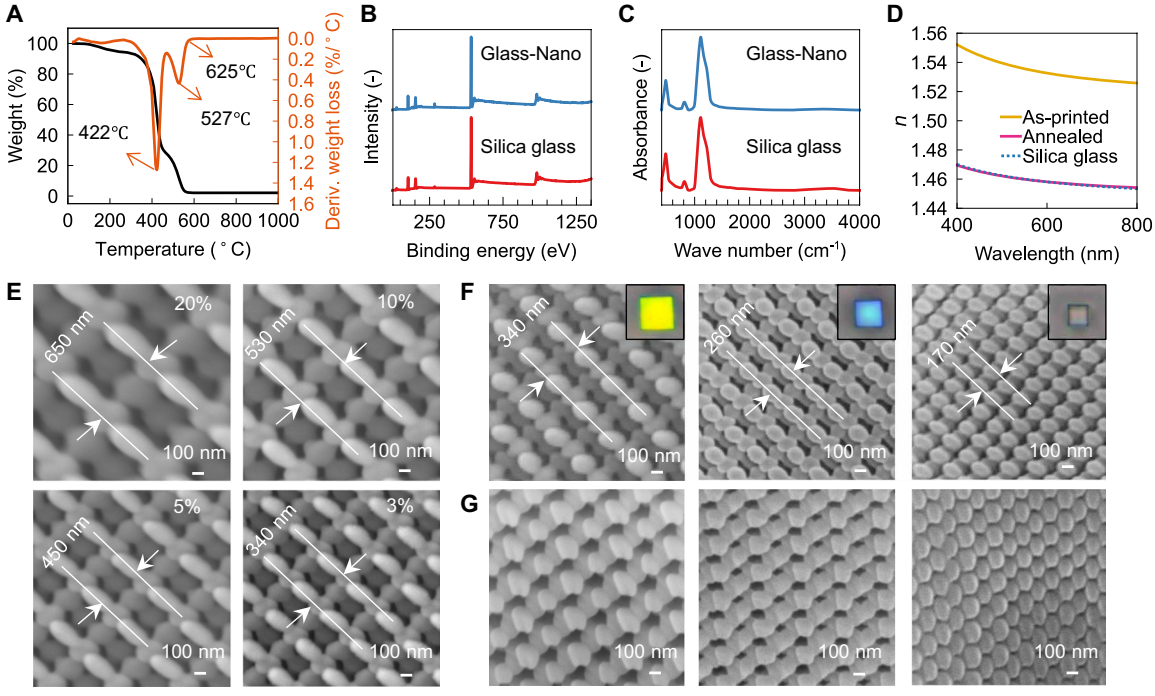

Fig. 2. Material characterization. (**A**) TGA of the polymerized Glass-Nano material in the air shows that the organic composition inside the material decompose completely at 625°C. (**B** and **C**) XPS and FTIR analysis show high purity of the Glass-Nano after sintering at 650°C. (**D**) The RI (*n*) of the sintered Glass-Nano material matches bulk silica glass perfectly and is ~5% lower than the as-printed (pre-sintered) material. (**E**) Top view SEM images of sintered 3D diamond PhCs printed from Glass-Nano resin with precursor concentrations of 20, 10, 5, and 3% respectively. (**F**) Top view SEM images of sintered 3D diamond PhCs with varying pitch. Insets in (F) are the corresponding optical micrographs. The PhCs shown in the insets have 20 units in the lateral direction. (**G**) Corresponding tilt view (45°) SEM images of (F).

sample (Fig. 2, B and C, and fig. S4). Energy-dispersive x-ray spectroscopy (EDS) shows the uniform distribution of silicon and oxygen in the sintered structure (fig. S5). Diffraction patterns in transmission electron microscopy (TEM) reveal the amorphous state of the sintered glass (fig. S6).

The as-printed polymer has an RI of ~1.53 at a wavelength of 532 nm (Fig. 2D). This RI is slightly higher than that of the resin as polymerization leads to an increase in RI (*42*). After sintering, the RI reduces to ~1.46 as the polymer composition is removed, closely matching that of standard silica glass. The sintered material shows a low extinction coefficient and high transmittance in the visible range (fig. S7). Atomic force microscopy shows the high smoothness of the sintered surface (fig. S8). By reducing the precursor concentration from 20 to 3%, the pitch of the sintered structure decreases from 650 to 330 nm (Fig. 2E), for the same nominal design and printing parameters. To achieve a high shrinkage ratio and high resolution, the 3% precursor resin was used in the following parts of this paper, which shows high uniformity in the top layers after sintering (fig. S9, A to D). Notably, reducing the precursor concentration further to 1% still produces highly uniform PhCs after sintering (fig. S9, F to J). To evaluate the printing resolution in 3D, we printed the PhCs with different pitches (fig. S10). In the as-printed PhCs, the features in the horizontal direction remain clear (fig. S10, A to C) as the pitch decreases from 1.65 to 0.85 μm. A horizontal pitch as small as 260 nm (Fig. 2F, middle) can be achieved after sintering, where the pitches in the vertical direction are clearly visible (Fig. 2G, middle). With further reduction of the pitch in the vertical direction, the features begin to merge when the initial pitch is 0.85 μm (fig. S10F). This limitation is due to the TPL printing resolution being lower in the vertical direction than in the horizontal direction, with the voxel shape having an aspect ratio of ~3.5 (*43*). After sintering, the structures with well-defined pitches show structural colors (Fig. 2F, insets), while the structure without internal air gaps (Fig. 2G, right) looks transparent (Fig. 2F, right inset), with weak scattering colors caused by the nano features on the top surface.

To understand the observation of high-reflectance features in PhCs with well-defined pitch (Figs. 1F and 2, F and G), we simulate the reflectance spectra of PhCs with varying layer numbers in the vertical direction (Fig. 3A). The peak reflectance increases with the number of layers, reaching nearly 100% when exceeding 20 layers. To test this experimentally, we printed 3D PhCs with 20, 30, 40, 50, and 60 layers in the vertical direction. After sintering, the first few layers near the substrate become distorted (fig. S11, A to E). As a result, the 20-layer PhC is substantially distorted overall, effectively collapsing after sintering (fig. S11A). A minimum of 40 layers was used for the subsequent studies, with the top 21 layers remaining uniform after sintering (fig. S11H). The uniformity could be further enhanced by introducing a sacrificial layer and transferring the structures to a nonstick substrate before sintering (*44*). Unlike previously reported low-RI 3D PhCs (*10*, *19*), which exhibited low reflectance in the 10 to 50% range, our glass 3D PhCs reach ~100% reflectance when the number of vertical stacking layers exceeds ~21 (Fig. 3B and fig. S11H). To analyze the reflectance at different angles, we measured the angle-resolved spectra of a 500-nm pitch fabricated PhC (Fig. 3C). The reflectance reaches ~100% reflectance within the −20° to 20° range, while the transmittance is <1% (Fig. 3, D and E).

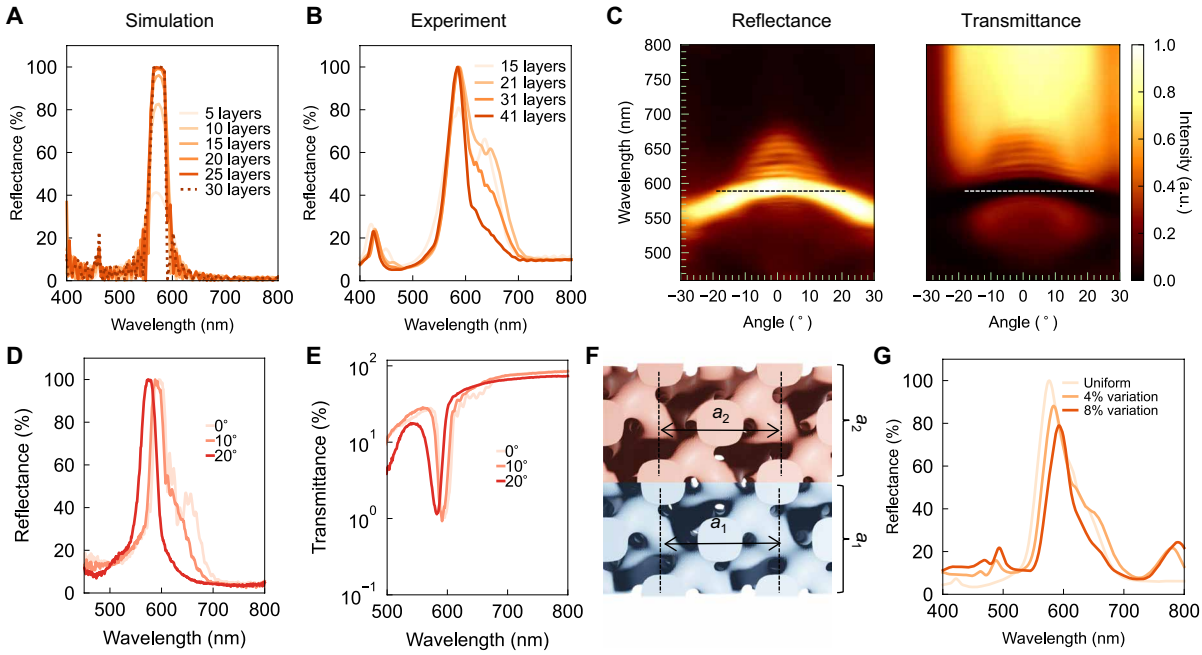

Fig. 3. Optical characterization of the glass PhCs. (**A**) Finite-difference time-domain (FDTD) simulated spectra of diamond PhCs with different layers. The diamond PhCs have a lattice constant of 500 nm, and a solid volume fraction of 30%. Here, one layer refers to one period of the (conventional) cubic PhC unit cell in the vertical direction. (**B**) Spectra of diamond PhCs with different uniform layers measured from an optical microscope (10 × 0.3 NA). The number of uniform layers is counted using the SEM images in fig. S11. (**C**) Measured angle-resolved reflectance and transmittance spectra of a diamond PhC with 31 uniform layers. The dashed lines indicate the formation of a partial bandgap in the −20° to 20° incidence angle range. (**D** and **E**) Measured reflectance and transmittance spectra of the diamond PhC in (C) at specific angles. (**F**) Side view schematic illustrates the change in uniformity within the design. In this design, diamond PhCs with slightly different lattice constants, a_1 and a_2, are used in alternating layers. Three cases are considered: $a_1 = 2.5$ μm, $a_2 = 2.5$ μm (uniform); $a_1 = 2.5$ μm, $a_2 = 2.6$ μm (4% variation); $a_1 = 2.5$ μm, $a_2 = 2.7$ μm (8% variation). (**G**) Measured optical spectra for PhCs with varying degrees of uniformity.

The observation of high reflectance in the −20° to 20° incidence angle range can be attributed to a partial bandgap in the projected band structure, as we discuss shortly. This effect is also a direct consequence of the type of PhC and its symmetry: Fabricating a gyroid PhC, a popular body-centered lattice motif in PhCs design (*45*), does not attain a similarly high or broad reflectance peak compared to our fabricated diamond-like PhCs. Angle-resolved spectra show that the high-reflectance region in the gyroid PhC is limited to ±10° (fig. S12A). As a result, the measured reflectance within the collection angle appears low (fig. S12B). The near-unity reflectance is also strongly affected by the uniformity of the PhCs. To illustrate this, we fabricated diamond PhCs with slightly different pitches in alternating layers (Fig. 3F). After printing with the same parameters, the samples were sintered (fig. S13), and the reflectance of the sintered PhCs was measured (Fig. 3G). The uniform sample shows ~100% reflectance around 580 nm. As nonuniformity increases, the reflectance decreases by as much as 20% for an 8% pitch deviation. The difference in PhC types, along with the nonuniformity, explains the low reflectance observed in previous reports for low-RI PhCs (*10*, *18*).

The existence of a high-reflectance region across a range of incidence angles can be understood directly from the band structure of the PhC (Fig. 4) by accounting for the surface termination along the [001] direction. The PhC has the symmetry of the zinc-blende structure (space group 216, $F\bar{4}3m$), related to the more familiar diamond structure (space group 227, $Fd\bar{3}m$) by the absence of an inversion center, with a face-centered cubic unit cell (Fig. 4B, inset). The associated bulk Brillouin zone (BZ) has the shape of a truncated octahedron (Fig. 4A, black). The bulk band structure (Fig. 4B) does not exhibit a complete gap, but the two lowest-frequency bands are disconnected from all higher-frequency bands at every wave vector **k**.

Unlike the infinitely extended structure associated with the bulk band structure, the fabricated PhCs are necessarily finite, as the incident light impinges on a [001]-terminated facet of the sample. In a zeroth-order diffraction approximation, the in-plane wave vectors (k_x, k_y) remain conserved at this interface, but incident light may couple to every out-of-plane wave vector k_z of the PhC band structure, i.e., k_z is not conserved. To capture this, we compute the [001]-projected band structure (Fig. 4C), obtained by stacking sweeps of the bulk band structure across points in the (conserved) in-plane surface BZ (Fig. 4A, blue), while sweeping the nonconserved wave vector k_z across its domain. The projected band structure exhibits a local gap at $\bar{\Gamma}$, corresponding to inhibited propagation for normally (i.e., along [001]) incident light. To understand the appearance of this local surface gap, despite the lack of a complete bulk gap, we note that the $\bar{\Gamma} = (0, 0, k_z)$ surface BZ point "projects through" the bulk band structure at Γ and X (every square facet of the truncated octahedron features a **k**-point that is symmetry related to the X point in Fig. 4A), each featuring large and overlapping gaps; their joint gap is limited by that at X, which extends from 560 to 590 nm, perfectly matching the local gap at $\bar{\Gamma}$.

The projected band structure can be related to the angle-resolved measurements by a simple geometric consideration. To illustrate this, we consider an incident plane wave of wavelength λ making a

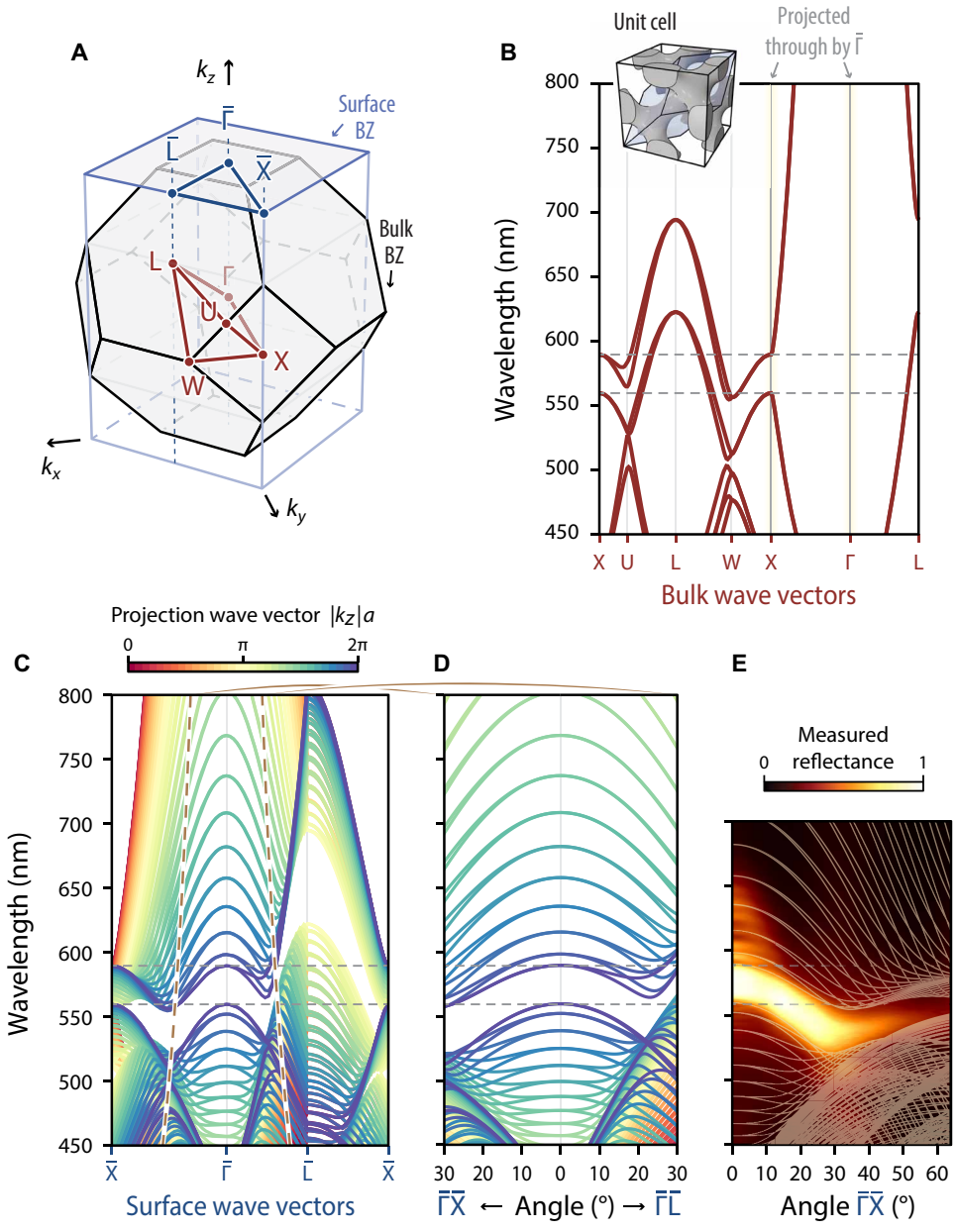

Fig. 4. Band structure analysis of [100]-terminated PhC sample. (**A**) Bulk and surface Brillouin zones (BZs) of the face-centered cubic PhC, with high-symmetry **k**-points highlighted for each. (**B**) Bulk band structure through high-symmetry **k**-path (inset: the conventional, cubic PhC unit cell; primitive unit cell in blue shading; cubic pitch, 500 nm; filling fraction, 30%). (**C**) The [001]-projected band structure. Each **k**-point in the surface BZ represents a sweep through the entire k_z domain (73 samples) for fixed in-plane wave vector (k_x, k_y); the association to a specific k_z value is indicated in color. The $\bar{\Gamma}$ point projects through the Γ and X bulk points from (B). The 30° incidence light cone is shown in dashed brown. (**D**) The [001]-terminated projected band structure cast to incidence angles. A partial gap exists for incidence angles from 0° to ~25° in both the $\overline{\Gamma X}$ and $\overline{\Gamma L}$ directions (corresponding to in-plane incidence along $\hat{\mathbf{y}}$ and $\hat{\mathbf{x}} + \hat{\mathbf{y}}$, respectively). (**E**) A comparison of the simulation (solid lines) and the experimentally measured reflectance (color map, as in Fig. 3C) for angles from 0° to 64° (measured data are shifted 20 nm down in wavelength).

polar angle ϑ to the [001]-normal, incident in the (y, z) plane with wave vector components in the (k_y, k_z) plane equaling $k_y = (2\pi/\lambda)\sin\vartheta$ and $k_z = (2\pi/\lambda)\cos\vartheta$. Within a zeroth-order diffraction approximation, k_y is conserved at the [001]-terminated PhC interface, such that incidence at ϑ implies coupling exclusively with surface BZ wave vectors at $k_x = (2\pi/\lambda)\sin\vartheta$. An analogous argument applies to any in-plane rotation of the incidence plane. This allows a recasting of the projected band structure from the surface BZ's (k_x, k_y) domain to the experimental domain spanned by a polar incidence angle ϑ and an in-plane direction (Fig. 4D). We observe excellent agreement between gaps in the angle-resolved projected band structure (Fig. 4D) and the high-reflectance regions of the angle-resolved reflectance measurements (Fig. 4E). Relative to the computed normal-incidence gap (560 to 590 nm), a ~20-nm shift and a negligible size

reduction is observed experimentally that is likely attributable to minor differences between fabricated and simulated geometries (e.g., the mid gap position is inversely proportional to the pitch, structural inhomogeneity reduces the gap size, and filling fraction affects both). Even fine features, such as the mini-bands observed above the high-reflectance gap in Fig. 3C, are reproduced qualitatively by the projected band structure via the spacing between k_z-sampled bands (the spacing is determined by the number of k_z samples; we take $2 \times 31 + 1$ samples across k_z, consistent with cyclic boundary conditions imposed on a 31-layer structure). The experimental mini-band spacings are smaller than the theoretical prediction, however, likely reflecting a small experimental symmetry breaking relative to space group 216, leading to splitting of otherwise near-degenerate projected bands.

Analogous reasoning allows us to infer the high-reflection spectral regions of PhCs with different termination facets directly from the bulk band structure, e.g., a [111]-terminated surface, corresponding to nonconserved wave vectors along [111], producing a projected band structure with surface BZ origin $\overline{\Gamma}$ projecting through the bulk $\mathbf{k}$-points Γ and L, with the gap at L (623 to 694 nm) limiting the projected gap and producing a red-shifted reflectance peak relative to the [001]-terminated surface. Similarly, a [120]-terminated surface projects W and Γ to $\overline{\Gamma}$, with the gap at W (513 to 556 nm) limiting the projected gap, producing a blue shift relative to the [001]-terminated surface.

Proceeding similarly, we analyze and compare the measured reflectance spectra of the fabricated gyroid PhC with band structure calculations in figs. S14 and 15. Despite the lack of perfect reflection in gyroid PhC, we again observe clear agreement between experiments and the band structure features from calculations.

DISCUSSION

Our work introduces a method for printing glass with ~100 nm feature sizes and nanoscale precision in three dimensions. A custom Glass-Nano resin was developed and characterized. 3D glass diamond PhCs were fabricated by using TPL followed by sintering in air. Unlike earlier demonstrations of low-index 3D PhCs, which have exhibited comparatively low reflectance, our glass PhCs achieve near-100% reflectance in the visible range within a wide window of collection angles. Numerical simulations reveal that the high-reflectance region coincides with a partial bandgap in the projected band structure, which inhibits light propagation in the PhCs across a wide range of incidence angles. This partial bandgap is particularly sensitive to the symmetry and geometry of the PhC design. In addition, achieving a high reflectance in this low-index setting, which associates with a longer penetration depth of light, requires both a large number of repeat units (>20) and a very high degree of uniformity of the fabricated structure. Our observation of near-100% reflectance and the excellent agreement between idealized-geometry band structure calculation and measured reflectance data demonstrate that our fabricated PhCs exhibit minimal and beyond state-of-the-art nonuniformity. The high-quality glass PhCs fabricated in this work are a notable example of how band structure engineering can achieve high-reflectance properties, even without the use of high-index materials. These findings open opportunities for the development of high-performance optical devices using low-RI materials, such as flexible and self-assembled systems.

MATERIALS AND METHODS

Materials

BPADA (average molecular weight, ~468), PETA, toluene, diphenyl (2,4,6-trimethylbenzoyl) phosphine oxide (TPO), propylene glycol monomethyl ether acetate (PGMEA), isopropyl alcohol (IPA), 3-(trimethoxysilyl) propyl methacrylate, acetic acid, and ethyl alcohol were purchased from Sigma-Aldrich. DETC was purchased from Exciton. MA0736 acryloxypropyl POSS cage mixture was purchased from Hybrid Plastics Inc. All chemicals were used as received.

Preparation of resin

For a resin with a 3% concentration of the precursor, 150 mg of MA0736, 300 mg of toluene, 1.42 g of PETA, 3.13 g of BPADA, and 50 mg of DETC were mixed and stirred with a magnetic rotor at room temperature (22°C) for 8 hours to obtain the homogeneous Glass-Nano resin. For bulk samples, a 2% mass ratio of TPO, instead of DETC, was added to cure the samples using an ultraviolet light source. Resins with other concentrations of the precursor were prepared using the same process (Supplementary Materials).

Additive manufacturing

Before printing, a silica substrate ($25 \times 25 \times 0.7$ mm^3, RI = 1.46) was treated with a solution of ethyl alcohol, acetic acid, 3-(trimethoxysilyl) propyl methacrylate, and deionized water mixture (*25*) to enhance adhesion. A drop of resin was then applied to the substrate and printed using a two-photon lithography system (Photonic Professional GT2, Nanoscribe GmbH, Germany) with a 63× objective lens [numerical aperture (NA) = 1.4] in a dip-in laser lithography configuration. The writing speed was set to 10 mm/s, and the laser power was adjusted between 10 and 15 mW. After printing, the sample was developed in PGMEA and IPA for 5 and 1 min, respectively. It was then rinsed with deionized water for 1 min and dried using a compressed air stream. The STL files used for printing were generated by the MSLattice software (*46*).

Sample sintering

The prepared samples were sintered in air using a Nabertherm P300 furnace, with the temperature increased at a rate of 2°C/min. After being held at elevated temperatures for 1 hour, the samples were cooled naturally to room temperature.

Materials characterization

The RI of the materials was measured by an ellipsometer (EP4, ACCURION, Germany). TGA was carried out with a TGA55 analyzer (TA Instruments) under an air atmosphere, where the samples were heated from room temperature to 1000°C at a rate of 2°C/min. Field emission scanning electron microscopy images were obtained using a JSM-7600F (JEOL, Japan) microscope. XPS analysis was performed using a Thermo Fisher Scientific K-Alpha system. FTIR spectroscopy was conducted using a Thermo Fisher Scientific Nicolet iS5 machine. TEM analysis was performed using a JEOL JEM-F200 system.

Optical characterization

Normal-incidence reflectance spectra were acquired using a 10× objective lens (NA = 0.3) mounted on a Nikon Eclipse LV100ND optical microscope, coupled with a CRAIC 508 PV microspectrophotometer and a Nikon DS-Ri2 camera. Spectra were normalized to a silver mirror reference.

Angle-resolved spectra were obtained through a custom-designed back focal plane microspectrometer. A 100× objective with a numerical aperture of 0.8 was used.

Band structure calculations

Photonic band structures were calculated using the MIT Photonic Bands (MPB) software (*47*), at a 32 by 32 by 32 resolution. The unit cell refractive profile $n(\mathbf{r})$ was specified using a level-set surface $n(\mathbf{r}) = 1 + \theta\left[\phi_0 - \phi(\mathbf{r})\right]\left(n_{SiO_2} - 1\right)$ parameterized by a level-set function $\phi(\mathbf{r}) = \cos 2\pi\tilde{x}\ \cos 2\pi\tilde{y}\ \cos 2\pi\tilde{z} - \sin 2\pi\tilde{x}\ \sin 2\pi\tilde{y}\ \sin 2\pi\tilde{z}$ and isolevel $\phi_0 = -0.34$ (filling fraction of 30%), with scaled coordinates $\tilde{\mathbf{r}} = \mathbf{r}/a$, pitch $a = 500$ nm (of the cubic unit cell), Heaviside function θ, and nondispersive RI $n_{SiO_2} = 1.46$ (RI of silica at 596 nm).

Supplementary Materials

This PDF file includes:

Supplementary Text
Figs. S1 to S15
Table S1

REFERENCES AND NOTES

1. F. Kotz, K. Arnold, W. Bauer, D. Schild, N. Keller, K. Sachsenheimer, T. M. Nargang, C. Richter, D. Helmer, B. E. Rapp, Three-dimensional printing of transparent fused silica glass. *Nature* **544**, 337–339 (2017).
2. J. T. Toombs, M. Luitz, C. C. Cook, S. Jenne, C. C. Li, B. E. Rapp, F. Kotz-Helmer, H. K. Taylor, Volumetric additive manufacturing of silica glass with microscale computed axial lithography. *Science* **376**, 308–312 (2022).
3. X. Wen, B. Zhang, W. Wang, F. Ye, S. Yue, H. Guo, G. Gao, Y. Zhao, Q. Fang, C. Nguyen, X. Zhang, J. Lou, J. Bao, J. T. Robinson, P. M. Ajayan, 3D-printed silica with nanoscale resolution. *Nat. Mater.* **20**, 1506–1511 (2021).
4. F. Kotz, A. S. Quick, P. Risch, T. Martin, T. Hoose, M. Thiel, D. Helmer, B. E. Rapp, Two-photon polymerization of nanocomposites for the fabrication of transparent fused silica glass microstructures. *Adv. Mater.* **33**, e2006341 (2021).
5. P.-H. Huang, M. Laakso, P. Edinger, O. Hartwig, G. S. Duesberg, L.-L. Lai, J. Mayer, J. Nyman, C. Errando-Herranz, G. Stemme, K. B. Gylfason, F. Niklaus, Three-dimensional printing of silica glass with sub-micrometer resolution. *Nat. Commun.* **14**, 3305 (2023).
6. M. Li, L. Yue, A. C. Rajan, L. Yu, H. Sahu, S. M. Montgomery, R. Ramprasad, H. J. Qi, Low-temperature 3D printing of transparent silica glass microstructures. *Sci. Adv.* **9**, eadi2958 (2023).
7. J. Bauer, C. Crook, T. Baldacchini, A sinterless, low-temperature route to 3D print nanoscale optical-grade glass. *Science* **380**, 960–966 (2023).
8. D. Zhu, S. Jiang, C. Liao, L. Xu, Y. Wang, D. Liu, W. Bao, F. Wang, H. Huang, X. Weng, L. Liu, J. Qu, Y. Wang, Ultrafast laser 3D nanolithography of fiber-integrated silica microdevices. *Nano Lett.* **24**, 9734–9742 (2024).
9. P. Ye, Z. Hong, D. A. Loy, R. Liang, Solvent-free silsesquioxane self-welding for 3D printing multi-refractive index glass objects. *Adv. Opt. Mater.* **12**, 2400783 (2024).
10. J. Fischer, M. Wegener, Three-dimensional direct laser writing inspired by stimulated-emission-depletion microscopy. *Opt. Mater. Express* **1**, 614–624 (2011).
11. Z. Gan, M. D. Turner, M. Gu, Biomimetic gyroid nanostructures exceeding their natural origins. *Sci. Adv.* **2**, e1600084 (2016).
12. Z. Gan, Y. Cao, R. A. Evans, M. Gu, Three-dimensional deep sub-diffraction optical beam lithography with 9 nm feature size. *Nat. Commun.* **4**, 2061 (2013).
13. Z. Cai, Z. Li, S. Ravaine, M. He, Y. Song, Y. Yin, H. Zheng, J. Teng, A. Zhang, From colloidal particles to photonic crystals: Advances in self-assembly and their emerging applications. *Chem. Soc. Rev.* **50**, 5898–5951 (2021).
14. G. Posnjak, X. Yin, P. Butler, O. Bienek, M. Dass, S. Lee, I. D. Sharp, T. Liedl, Diamond-lattice photonic crystals assembled from DNA origami. *Science* **384**, 781–785 (2024).
15. B. R. Sveinbjörnsson, R. A. Weitekamp, G. M. Miyake, Y. Xia, H. A. Atwater, R. H. Grubbs, Rapid self-assembly of brush block copolymers to photonic crystals. *Proc. Natl. Acad. Sci. U.S.A.* **109**, 14332–14336 (2012).
16. A. Urbas, R. Sharp, Y. Fink, E. L. Thomas, M. Xenidou, L. J. Fetters, Tunable block copolymer/homopolymer photonic crystals. *Adv. Mater.* **12**, 812–814 (2000).
17. Y. Huang, J. Zhou, B. Su, L. Shi, J. Wang, S. Chen, L. Wang, J. Zi, Y. Song, L. Jiang, Colloidal photonic crystals with narrow stopbands assembled from low-adhesive superhydrophobic substrates. *J. Am. Chem. Soc.* **134**, 17053–17058 (2012).
18. H. K. Raut, H. Wang, Q. Ruan, H. Wang, J. G. Fernandez, J. K. Yang, Hierarchical colorful structures by three-dimensional printing of inverse opals. *Nano Lett.* **21**, 8602–8608 (2021).
19. Y. Liu, H. Wang, J. Ho, R. C. Ng, R. J. Ng, V. H. Hall-Chen, E. H. Koay, Z. Dong, H. Liu, C.-W. Qiu, J. R. Greer, J. K. W. Yang, Structural color three-dimensional printing by shrinking photonic crystals. *Nat. Commun.* **10**, 4340 (2019).
20. A. Vyatskikh, R. C. Ng, B. Edwards, R. M. Briggs, J. R. Greer, Additive manufacturing of high-refractive-index, nanoarchitected titanium dioxide for 3D dielectric photonic crystals. *Nano Lett.* **20**, 3513–3520 (2020).
21. J. Fischer, M. Wegener, Three-dimensional optical laser lithography beyond the diffraction limit. *Laser Photonics Rev.* **7**, 22–44 (2013).
22. W. Zhang, J. Min, H. Wang, H. Wang, X. L. Li, S. T. Ha, B. Zhang, C.-F. Pan, H. Li, H. Liu, H. Yin, X. Yang, S. Liu, X. Xu, C. He, H. Y. Yang, J. K. W. Yang, Printing of 3D photonic crystals in titania with complete bandgap across the visible spectrum. *Nat. Nanotechnol.* **19**, 1813–1820 (2024).
23. M. Kadic, G. W. Milton, M. van Hecke, M. Wegener, 3D metamaterials. *Nat. Rev. Phys.* **1**, 198–210 (2019).
24. W. Zhang, H. Wang, H. Wang, J. Y. E. Chan, H. Liu, B. Zhang, Y.-F. Zhang, K. Agarwal, X. Yang, A. S. Ranganath, H. Y. Low, Q. Ge, J. K. W. Yang, Structural multi-colour invisible inks with submicron 4D printing of shape memory polymers. *Nat. Commun.* **12**, 112 (2021).
25. W. Zhang, H. Wang, A. T. Tan, A. Sargur Ranganath, B. Zhang, H. Wang, J. Y. E. Chan, Q. Ruan, H. Liu, S. T. Ha, D. Wang, V. K. Ravikumar, H. Y. Low, J. K. W. Yang, Stiff shape memory polymers for high-resolution reconfigurable nanophotonics. *Nano Lett.* **22**, 8917–8924 (2022).
26. W. Wang, B. Zhou, S. Xu, Z. Yang, Q. Zhang, Recent advances in soft optical glass fiber and fiber lasers. *Prog. Mater. Sci.* **101**, 90–171 (2019).
27. X. He, B. Zhang, Q. Liu, H. Chen, J. Cheng, B. Jian, H. Yin, H. Li, K. Duan, J. Zhang, Q. Ge, Highly conductive and stretchable nanostructured ionogels for 3D printing capacitive sensors with superior performance. *Nat. Commun.* **15**, 6431 (2024).
28. Q. Ge, Z. Chen, J. Cheng, B. Zhang, Y.-F. Zhang, H. Li, X. He, C. Yuan, J. Liu, S. Magdassi, S. Qu, 3D printing of highly stretchable hydrogel with diverse UV curable polymers. *Sci. Adv.* **7**, eaba4261 (2021).
29. S. C. Mannsfeld, B. C. Tee, R. M. Stoltenberg, C. V. H. Chen, S. Barman, B. V. Muir, A. N. Sokolov, C. Reese, Z. Bao, Highly sensitive flexible pressure sensors with microstructured rubber dielectric layers. *Nat. Mater.* **9**, 859–864 (2010).
30. C. B. Cooper, S. E. Root, L. Michalek, S. Wu, J.-C. Lai, M. Khatib, S. T. Oyakhire, R. Zhao, J. Qin, Z. Bao, Autonomous alignment and healing in multilayer soft electronics using immiscible dynamic polymers. *Science* **380**, 935–941 (2023).
31. Z. Yu, L. Michalek, Q. Liu, Y. Wu, H. Kim, P. Sayavong, W. Yu, D. Zhong, C. Zhao, Z. Yu, J. A. Chiong, H. Gong, X. Ji, D. Liu, S. Zhang, N. Prine, Z. Zhang, W. Wang, J. B.-H. Tok, X. Gu, Y. Cui, J. Kang, Z. Bao, Environmentally stable and stretchable polymer electronics enabled by surface-tethered nanostructured molecular-level protection. *Nat. Nanotechnol.* **18**, 1175–1184 (2023).
32. Y. Cho, S. Y. Lee, L. Ellerthorpe, G. Feng, G. Lin, G. Wu, J. Yin, S. Yang, Elastoplastic inverse opals as power-free mechanochromic sensors for force recording. *Adv. Funct. Mater.* **25**, 6041–6049 (2015).
33. J. Bürger, V. Schalles, J. Kim, B. Jang, M. Zeisberger, J. Gargiulo, L. d. S. Menezes, M. A. Schmidt, S. A. Maier, 3D-nanoprinted antiresonant hollow-core microgap waveguide: An on-chip platform for integrated photonic devices and sensors. *ACS Photonics* **9**, 3012–3024 (2022).
34. M. Mettry, M. A. Worthington, B. Au, J.-B. Forien, S. Chandrasekaran, N. A. Heth, J. J. Schwartz, S. Liang, W. Smith, J. Biener, S. K. Saha, J. S. Oakdale, Refractive index matched polymeric and preceramic resins for height-scalable two-photon lithography. *RSC Adv.* **11**, 22633–22639 (2021).
35. A. Vyatskikh, S. Delalande, A. Kudo, X. Zhang, C. M. Portela, J. R. Greer, Additive manufacturing of 3D nano-architected metals. *Nat. Commun.* **9**, 593 (2018).
36. H. Wang, W. Zhang, D. Ladika, H. Yu, D. Gailevičius, H. Wang, C. F. Pan, P. N. S. Nair, Y. Ke, T. Mori, J. Y. E. Chan, Q. Ruan, M. Farsari, M. Malinauskas, S. Juodkazis, M. Gu, J. K. W. Yang, Two-photon polymerization lithography for optics and photonics: Fundamentals, materials, technologies, and applications. *Adv. Funct. Mater.* **33**, 2214211 (2023).
37. W. Deng, S. Kumar, A. Vallone, D. M. Kochmann, J. R. Greer, AI-enabled materials design of non-periodic 3D architectures with predictable direction-dependent elastic properties. *Adv. Mater.* **36**, e2308149 (2024).
38. L.-Y. Hsu, S. G. Melo, C. Vazquez-Martel, C. A. Spiegel, F. Ziebert, U. S. Schwarz, E. Blasco, Alignment and actuation of liquid crystals via 3D confinement and two-photon laser printing. *Sci. Adv.* **10**, eadq2597 (2024).
39. S. Daqiqeh Rezaei, Z. Dong, J. Y. E. Chan, J. Trisno, R. J. H. Ng, Q. Ruan, C.-W. Qiu, N. A. Mortensen, J. K. Yang, Nanophotonic structural colors. *ACS Photonics* **8**, 18–33 (2021).
40. K. Li, T. Li, T. Zhang, H. Li, A. Li, Z. Li, X. Lai, X. Hou, Y. Wang, L. Shi, M. Li, Y. Song, Facile full-color printing with a single transparent ink. *Sci. Adv.* **7**, eabh1992 (2021).

41. J. Hou, M. Li, Y. Song, Patterned colloidal photonic crystals. *Angew. Chem. Int. Ed. Engl.* **57**, 2544–2553 (2018).
42. S. Dottermusch, D. Busko, M. Langenhorst, U. W. Paetzold, B. S. Richards, Exposure-dependent refractive index of nanoscribe IP-dip photoresist layers. *Opt. Lett.* **44**, 29–32 (2018).
43. S. Hengsbach, A. D. Lantada, Rapid prototyping of multi-scale biomedical microdevices by combining additive manufacturing technologies. *Biomed. Microdevices* **16**, 617–627 (2014).
44. T. Mori, H. Wang, W. Zhang, C. C. Ser, D. Arora, C.-F. Pan, H. Li, J. Niu, M. Rahman, T. Mori, H. Koishi, J. K. W. Yang, Pick and place process for uniform shrinking of 3D printed micro-and nano-architected materials. *Nat. Commun.* **14**, 5876 (2023).
45. M. Maldovan, A. Urbas, N. Yufa, W. Carter, E. Thomas, Photonic properties of bicontinuous cubic microphases. *Phys. Rev. B* **65**, 165123 (2002).
46. O. Al-Ketan, R. K. Abu Al-Rub, MSLattice: A free software for generating uniform and graded lattices based on triply periodic minimal surfaces. *Mater. Des. Process. Commun.* **3**, e205 (2021).
47. S. G. Johnson, J. D. Joannopoulos, Block-iterative frequency-domain methods for Maxwell's equations in a planewave basis. *Opt. Express* **8**, 173–190 (2001).

Acknowledgments
Funding: J.K.W.Y. acknowledges National Research Foundation (NRF) Singapore (NRF-NRFI06-2020-0005) and Singapore MTC-Programmatic grant no. M21J9b0085. This research is also partially supported by grants from the National Research Foundation, Prime Minister's Office, Singapore under its Campus for Research Excellence and Technological Enterprise (CREATE) program. J.K.W.Y. acknowledges support from the guest professor program of the Otto Mønsted Foundation (grant no. ~23-12-1947). T.C. acknowledges the support of a research grant (project no. 42106) from Villum Fonden. **Author contributions:** Conceptualization: W.Z., Hongtao Wang, Hao Wang, T.C., and J.K.W.Y. Investigation: W.Z., Hongtao Wang, Hao Wang, S.T.H., and J.K.W.Y. Methodology: W.Z., Hongtao Wang, Hao Wang, L.C., C.-F.P., B.W., M.A.R., Q.R., and T.C. Resources: W.Z., Hongtao Wang, Hao Wang, and J.K.W.Y. Data curation: W.Z., Hongtao Wang, and Hao Wang. Validation: W.Z., Hongtao Wang, Hao Wang, S.T.H., T.C., and J.K.W.Y. Formal analysis: W.Z., Hongtao Wang, Hao Wang, S.T.H., L.C., X.L.L., Y.K., and T.C. Visualization: W.Z., Hongtao Wang, Hao Wang, L.C., X.Y., T.C., and J.K.W.Y. Software: Hongtao Wang, L.C., and T.C. Funding acquisition: J.K.W.Y. Supervision: J.K.W.Y. Project administration: J.K.W.Y. Writing—original draft: W.Z., C.-F.P., and T.C. Writing—review and editing: W.Z., Hongtao Wang, Hao Wang, S.T.H., X.L.L., C.-F.P., B.W., M.A.R., Y.K., Q.R., X.Y., T.C., and J.K.W.Y. All authors discussed the results and commented on the manuscript. **Competing interests:** The authors declare that they have no competing interests. **Data and materials availability:** All data needed to evaluate the conclusions in the paper are present in the paper and/or the Supplementary Materials.

Submitted 2 December 2024
Accepted 18 April 2025
Published 23 May 2025
10.1126/sciadv.adv0267